Ligand impact on reactive oxygen species generation of Au10 and Au25 nanoclusters upon one- and two-photon excitation

Hussein Fakhouri, Martina Perić Bakulić, Issan Zhang, Hao Yuan, Dipankar Bain, Fabien Rondepierre, Pierre-François Brevet, Željka Sanader Maršić, Rodolphe Antoine, Vlasta Bonačić-Koutecký, et al.

communications chemistry

ARTICLE

https://doi.org/10.1038/s42004-023-00895-5 OPEN

Ligand impact on reactive oxygen species generation of Au_{10} and Au_{25} nanoclusters upon one- and two-photon excitation

Hussein Fakhouri[1,2], Martina Perić Bakulić[2,3], Issan Zhang[4], Hao Yuan[1], Dipankar Bain[1], Fabien Rondepierre[1], Pierre-François Brevet[1], Željka Sanader Maršić[5], Rodolphe Antoine[1,8✉], Vlasta Bonačić-Koutecký[2,6,7,8✉] & Dusica Maysinger[4,8✉]

In photodynamic therapy (PDT), light-sensitive photosensitizers produce reactive oxygen species (ROS) after irradiation in the presence of oxygen. Atomically-precise thiolate-protected gold nanoclusters are molecule-like nanostructures with discrete energy levels presenting long lifetimes, surface biofunctionality, and strong near-infrared excitation ideal for ROS generation in PDT. We directly compare thiolate-gold macromolecular complexes (Au_{10}) and atomically-precise gold nanoclusters (Au_{25}), and investigate the influence of ligands on their photoexcitation. With the ability of atomically-precise nanochemistry, we produce $Au_{10}SG_{10}$, $Au_{10}AcCys_{10}$, $Au_{25}SG_{18}$, and $Au_{25}AcCys_{18}$ (SG: glutathione; AcCys: N-acetyl-cysteine) fully characterized by high-resolution mass spectrometry. Our theoretical investigation reveals key factors (energetics of excited states and structural influence of surface ligands) and their relative importance in singlet oxygen formation upon one- and two-photon excitation. Finally, we explore ROS generation by gold nanoclusters in living cells with one- and two-photon excitation. Our study presents in-depth analyses of events within gold nanoclusters when photo-excited both in the linear and nonlinear optical regimes, and possible biological consequences in cells.

[1] Institut Lumière Matière, University of Lyon, Université Claude Bernard Lyon 1, CNRS, F-69622 Lyon, France. [2] Center of Excellence for Science and Technology, Integration of Mediterranean Region (STIM), Faculty of Science, University of Split, Ruđera Boškovića 33, 21000 Split, Croatia. [3] Faculty of Chemistry and Technology, University of Split, Rudera Boskovica 35, 21000 Split, Croatia. [4] Department of Pharmacology and Therapeutics, McGill University, 3655 Promenade Sir-William-Osler, H3G 1Y6 Montreal, Canada. [5] Faculty of Science, University of Split, Rudera Boskovica 33, 21000 Split, Croatia. [6] Interdisciplinary Center for Advanced Science and Technology (ICAST), University of Split, Meštrovićevo šetalište 45, 21000 Split, Croatia. [7] Chemistry Department, Humboldt University of Berlin, Brook-Taylor-Strasse 2, 12489 Berlin, Germany. [8] These authors contributed equally: Rodolphe Antoine, Vlasta Bonačić-Koutecký, Dusica Maysinger. ✉email: rodolphe.antoine@univ-lyon1.fr; vbk@cms.hu-berlin.de; dusica.maysinger@mcgill.ca

Photodynamic therapy (PDT) is a powerful therapeutic method using a light-sensitive compound or structure, commonly named a photosensitizer to produce reactive oxygen species (ROS)[1] after irradiation with light in the presence of oxygen[2]. A photosensitizer molecule is usually irradiated by visible or near-infrared (NIR) light. A photosensitizer absorbs the light and is excited to its singlet state. The excited state electrons undergo intersystem crossing to a lower energy, but longer-lived triplet state, from which ROS or reactive molecular transients are generated (Fig. 1). The photochemical reactions proceed via a type I (by electron transfer) or type II (by energy transfer) mechanism and require close proximity between the photosensitizer and molecular oxygen. The photosensitizer should possess high light absorption coefficients, ideally at long wavelength radiations (red or near-infrared), long lifetime (to allow high intersystem crossing efficiencies), and good biocompatibility (in the absence of light). Many structures, ranging from single organic-based molecules, thiolate-metal complexes[3] to tailor-made nanomaterials, have been used as photosensitizers[4]. Atomically precise thiolate (SR)-protected gold nanoclusters ($Au_n(SR)_m$) are molecule-like nanostructures[5,6] presenting long lifetimes, surface biofunctionality, and strong NIR excitation that are thus ideal candidates for generating ROS—in particular singlet oxygen ($^1O_2$). It was shown by pioneering studies that $Au_{25}(SR)_{18}$ excited either by light[7,8] or by ultrasound[9] can donate enough energy to convert $^3O_2$ into $^1O_2$. In addition, atomically precise gold nanoclusters (mainly protected by proteins) have been recently proposed as Type-I-Type-II sensitizers for potential use in PDT either using one-photon red or NIR light[10–14], or two-photon excitation[8,15].

A few experimental studies have tried to address size effects either between different Au_nSR_m atomically precise nanoclusters[16] or between molecule-like clusters and plasmonic gold nanoparticles[8]. However, to our knowledge, no direct comparison between thiolate-gold macromolecular complexes and atomically precise gold nanoclusters has been explored. Thus, Au_{10} (thiolate-gold macromolecular complexes) and Au_{25} (atomically precise gold nanoclusters) were chosen to highlight how discrete energy levels and the nature of excited states may influence the photosensitizing abilities of atomically precise gold clusters to produce ROS (in particular $^1O_2$). Indeed, as illustrated in Fig. 1, an efficient photosensitizer for $^1O_2$ production requires a high triplet-state yield with a triplet-state energy higher than the energy of $^1O_2$ (0.98 eV) for efficient energy transfer to $^3O_2$. From this viewpoint, the optical gap of thiolate-protected $Au_{25}(SR)_{18}$ nanoclusters is slightly higher than 1 eV[17,18], and due to the long-lifetime, the triplet-state efficiency is high. This is mainly due to the strong interaction between core states in the gold core and the surface states at the Au-S interface. In contrast, the optical gap of $Au_{10}SR_{10}$ is much higher, at ~2.6–2.7 eV[17,19,20], and therefore it can also donate enough energy to form $^1O_2$. However, as opposed to $Au_{25}(SR)_{18}$ containing 8 confined electrons in the gold core, $Au_{10}(SR)_{10}$ presents a catenane structure with zero confined electrons[19–22]. Aurophilic Au···Au subunits with neighboring sulfur atoms in catenane structures of Au_{10} nanoclusters play a key role in the photophysical processes[19].

In addition to the effect of molecular-like properties of ultra-small nanoclusters, our aim is to evaluate the influence of ligands on the efficiency of photoexcited gold clusters to produce ROS. Wu and Jin did a seminal work demonstrating that ligands play a key role on the photoluminescence efficiencies of thiolate-protected nanoclusters[23]. Since ROS generation involves subtle photophysical relaxation processes in excited states, it is thus postulated that ligands should also play a role in the ROS generation of photoexcited nanoclusters. However, very few studies explore the possible impact of ligands, mainly focusing on Au_{25} capped with thiolate molecules (captopril, 4-mercaptobenzoic acid), peptides (glutathione) or proteins (albumin)[16,24].

In this work, with the ability of atomically precise nanochemistry, our aim is to produce $Au_{10}SG_{10}$, $Au_{10}AcCys_{10}$, $Au_{25}SG_{18}$ and $Au_{25}AcCys_{18}$, (SG: glutathione; AcCys: N-acetylcysteine) which are fully characterized by high-resolution mass spectrometry[25]. Reactive oxygen species generation studies were conducted on Au_{10} and Au_{25} nanoclusters with different mode of photoexcitation (either by one-photon excitation with visible light or by two-photon excitation with NIR light). The effectiveness of such nanoclusters as photosensitizers has been evaluated in solution with an indirect singlet oxygen detection method under visible excitation using a continuous wave laser emitting at 473 nm and under NIR excitation using a femtosecond laser emitting at 780 nm and 720 nm. In such scenario, only the first excited states of nanoclusters are supposed to be involved in the photoexcitation process. Singlet oxygen formation is a low energy process (0.98 eV), the gap between singlet (S) and triplet (T) states as well as the energy of the lowest T_1 states are key factors to evaluate the possible difference between Au_{10} and Au_{25} to produce single oxygen. Therefore, in parallel to this experimental investigation, the excited states involved in the photoexcitation and de-excitation processes are discussed based on results of time-dependent density functional theory (TDDFT) method. In

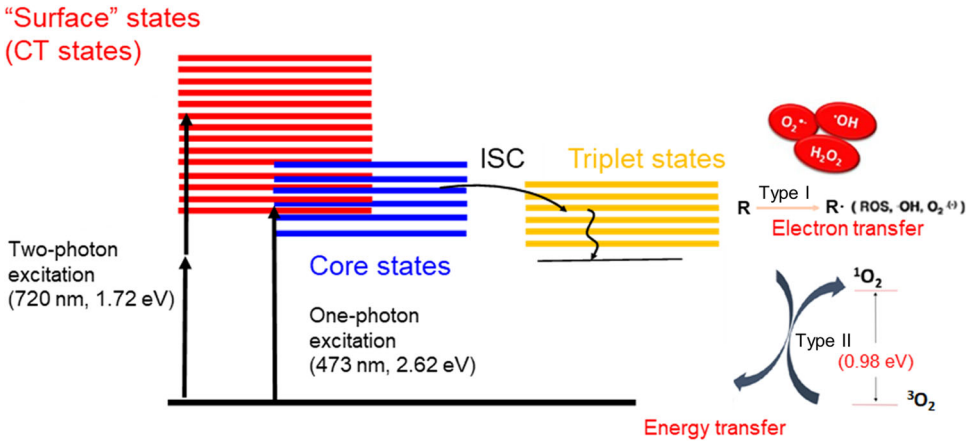

Fig. 1 Type I and type II mechanism of ROS generation using photoexcited gold nanoclusters (upon one- and two-photon excitation). CT charge transfer, ISC intersystem crossing, $O_2^{\cdot-}$, superoxide anion, •OH hydroxyl radical, H_2O_2 hydrogen peroxide, $^3O_2$ triplet state oxygen (molecular oxygen), $^1O_2$ singlet oxygen.

order to address the possible role of surface ligands on the efficiency to produce singlet oxygen, such theoretical modeling was conducted by taking into account fully explicit ligands (glutathione and N-acetyl-cysteine) on Au_{10} and Au_{25} nanoclusters. The choice of ligands as protecting agents for gold clusters was mainly driven by their biocompatibility and their similarity from a biological point of view. Indeed, acetyl-cysteine serves as a precursor of glutathione biosynthesis[26]. Both ligands are endogenous compounds in cells and as such do not cause any toxicity under low micromolar concentrations, even when bound to gold nanoclusters. Our recent study provided some insights into the impact of Au_{10} nanoclusters on human microglia and interaction with high mobility group box 1 (HMGB1)[27].

This joint experimental-theoretical investigation will allow to gain better insight into key factors (energetics of excited states and structural influence of surface ligands), as well as their relative importance involved in singlet oxygen formation upon photoexcitation in the visible and NIR range. In order to open this joint experimental-theoretical investigation for application-oriented perspectives, we carried out live cell imaging to explore the ability of Au_{10} and Au_{25} nanoclusters to generate ROS in cells stimulated by one- and two-photon excitation. We studied human microglia following treatments with Au_{10} and Au_{25} nanoclusters protected with two ligands (glutathione and acetyl-cysteine). In addition, our study presented herein provides in-depth analyses of events taking place within gold nanoclusters when photoexcited and their possible biological consequences in living cells.

Results

Singlet oxygen generation in metal nanoclusters excited by visible (one-photon excitation) and IR (two-photon excitation) light in solution. The indirect method was used to quantify singlet oxygen generation by photoexcited nanoclusters in solution. 1,3-diphenylisobenzofuran (DPBF) is known to be highly reactive toward singlet oxygen, forming endoperoxides (with different absorption properties, in particular at 412 nm) that can be used as optical probe[28]. The nanoclusters and DPBF can be excited simultaneously to generate and detect singlet oxygen. The generation of singlet oxygen was triggered by excitation of the nanoclusters with a continuous wave laser emitting at 473 nm with different times of exposure. The change in the absorption of DPBF was monitored over time at 412 nm[8]. The rate of $^1O_2$ generation was obtained by the initial DPBF concentration change over time ($\Delta[DPBF]_{0-15\,min}/\Delta t$) divided by the concentration of the nanoclusters. The rate of $^1O_2$ generation is presented in Table 1 for all four gold nanoclusters. The atomic precision of as-synthesized gold nanoclusters was examined by high-resolution mass spectrometry (Supplementary Fig. 1) while the feature absorption bands were verified by UV–vis absorption spectra (Supplementary Fig. 2). Absorption spectra and change in the absorption of DPBF monitored over time are presented in the Supplementary Fig. 3. Au_{25} has better efficiency to produce $^1O_2$ in solution than Au_{10}. For a given cluster size, acetyl-cysteine further enhances ROS generation efficiency as compared to glutathione (Table 1). To demonstrate the efficiency of gold nanoclusters for $^1O_2$ production, we compared $^1O_2$ production by gold nanoclusters to that of the conventional dye photosensitizer new methylene blue (NMB)[7]. A superior $^1O_2$ production efficiency was observed for $Au_{25}AcCys_{18}$ compared to NMB (Table 1). Of note, a superior $^1O_2$ production efficiency for $Au_{25}Cap_{t18}$ clusters compared to that of NMB was already reported[7]. Clearly at 473 nm, Au_{10} is a weakly absorbing species as compared to Au_{25}. This is even more dramatic in the nonlinear optical (NLO) regime upon excitation close to 800 nm (see reported two-photon absorption cross sections for Au_{10} and Au_{25})[19,29,30]. And therefore, the $^1O_2$ generation rate also depends on the absorbance of nanoclusters at the used laser light. We thus provide as Supplementary Table 1, the normalized $^1O_2$ generation rate of gold nanoclusters and NMB by absorbance at 473 nm. And clearly Au_{10} become more efficient than Au_{25} taking into account their absorbance at 473 nm. Photoluminescence lifetimes of the four gold nanoclusters was measured to reveal the electron states of these nanoclusters (Supplementary Fig. 4).

Theoretical study of the structural and ligand effects on singlet and triplet excited states of Au_{10} and Au_{25} nanoclusters with explicit acetyl-cysteine and glutathione ligands. The aim of the theoretical investigation is to propose ligands and size of gold nanoclusters that will allow efficient generation of singlet oxygen for potential use in photodynamic therapy. For this purpose, the explicit treatment of ligands for acetyl-cysteine and glutathione has been introduced in order to compare their influence on H-bond network.

Two cluster sizes, Au_{10} and Au_{25}, with different structural properties and two types of ligands, AcCys and SG, are shown in Figs. 2 and 3. The Au_{10} nanocluster has a catenane type structure with interlocked ring motifs connected by Au···Au bond, whereas the Au_{25} nanocluster has a core with delocalized electrons protected by ligands. The two types of ligands are characterized as flexible (AcCys) or bulky (SG), with different flexibilities due to different H-bond networks. The greater flexibility realized by AcCys ligands allows for the transitions from singlet to triplet states. The influence of cluster size (Au_{10} vs Au_{25}), along with

Table 1 Singlet oxygen generation rate of metal nanoclusters and dye photosensitizer under continuous wave 473 nm irradiation.

Photosensitizer	Emission peak	Quantum Yield	Long lifetime component (ns) (relative percentage of long lifetime component vs total lifetime)	$^1O_2$ generation rate ($^1O_2$ per cluster per min) @473 nm continuous wave laser irradiation
$Au_{10}SG_{10}$	615 nm	$<10^{-4}$ (ref. [17])	767 (15%)	1.07 ± 0.06
$Au_{10}AcCys_{10}$	605 nm	$<2.5\times10^{-5}$ (this work)*	680 (17.86%)	1.09 ± 0.18
$Au_{25}SG_{18}$	~815 nm	10^{-3} (ref. [17])	883 (6%)	1.86 ± 0.06
$Au_{25}AcCys_{18}$	~820 nm	1.2×10^{-4} (this work)*	812 (38%)	2.71 ± 0.20
NMB	652 nm	0.04 (ref. [56])	33 (100%)	2.28 ± 0.11

*The quantum yield of $Au_{25}AcCys_{18}$ ($Au_{10}AcCys_{10}$) was estimated using the reference method and $Au_{25}SG_{18}$ ($Au_{10}SG_{10}$) as the reference. Standard error for quantum yield is 10%.

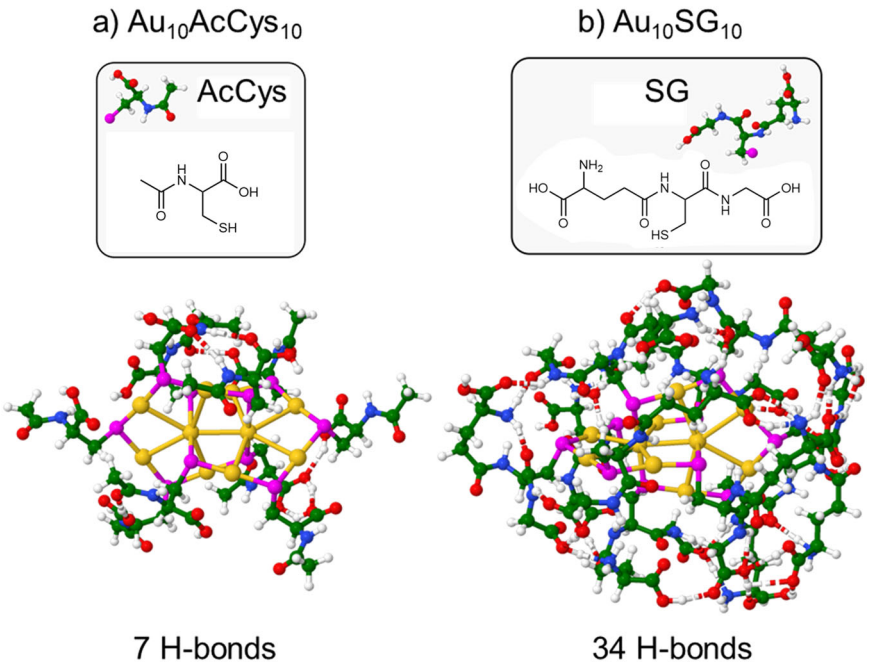

Fig. 2 Comparison of $Au_{10}AcCys_{10}$ and $Au_{10}SG_{10}$ illustrating ligand effects by hydrogen bonding network. Structures are presented for **a** $Au_{10}AcCys_{10}$ and **b** $Au_{10}SG_{10}$. Gold atoms in structures are labeled yellow. Ligands are shown in windows. For details on structures optimization see Computational Approach. SG glutathione, AcCys N-acetyl-cysteine.

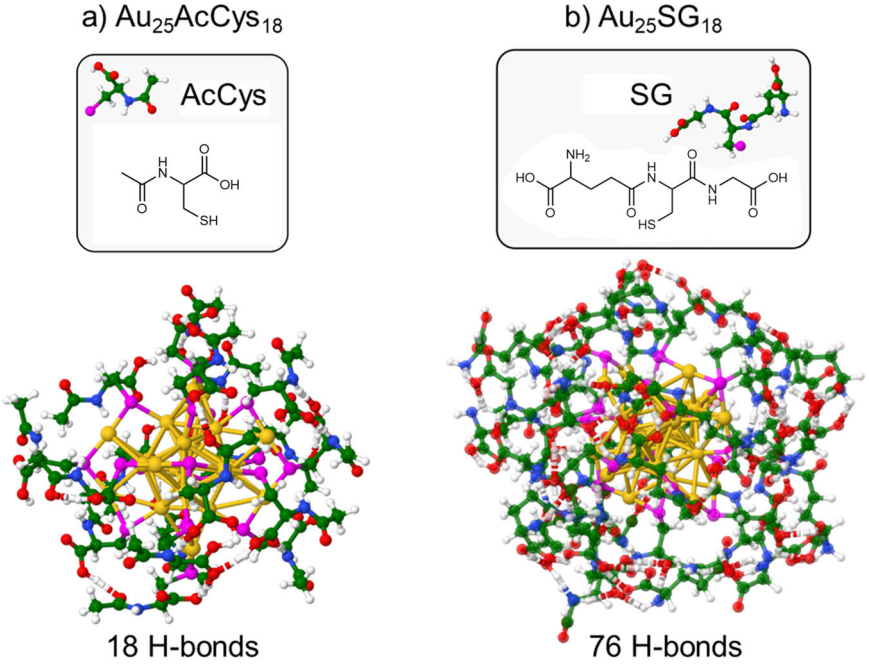

Fig. 3 Comparison of $Au_{25}AcCys_{18}$ and $Au_{25}SG_{18}$ illustrating ligand effects by hydrogen bonding network. Structures are presented for **a** $Au_{25}AcCys_{18}$ and **b** $Au_{25}SG_{18}$. Gold atoms in structures are labeled yellow. Ligands are shown in windows. For details on structures optimization see Computational Approach. SG glutathione, AcCys N-acetyl-cysteine.

structural properties in size regime in which each atom counts, changes drastically the relative energies of singlet-triplet states, as shown in Figs. 4 and 5 for the different ligands. This clearly evidences the advantage of $Au_{25}AcCys_{18}$ species for applications, given their close energies of singlet and triplet states and smaller number of H-bonds, promoting relaxation effects through intersystem crossing.

In the case of $Au_{10}AcCys_{10}$ and $Au_{10}SG_{10}$, excitations within the first three singlet and triplet states involve transitions between occupied and unoccupied molecular orbitals all localized at catenane bonds of interlocked ring motifs, as shown in the Supplementary Fig. 5a, b. The influence of ligands is negligible. Excitations within the first three singlet and triplet states of $Au_{25}AcCys_{18}$ and $Au_{25}SG_{18}$ species involve molecular orbitals of

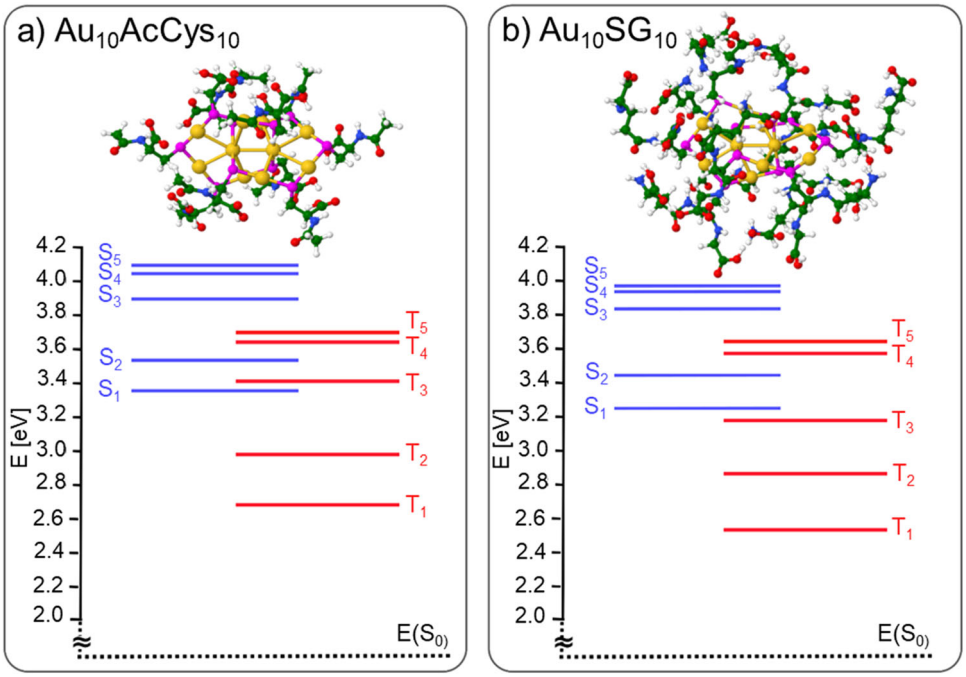

Fig. 4 Time-dependent density functional theory (TDDFT) energies for singlets (S_n, $n = 1$–5) and triplets (T_n, $n = 1$–5) states. TDDFT energies are shown for **a** $Au_{10}AcCys_{10}$ and **b** $Au_{10}SG_{10}$. Singlet-triplet (E_{S1}-E_{T1}) energy gaps are: $\Delta E_{S\text{-}T}$ ($Au_{10}AcCys_{10}$) = 0.68 eV and $\Delta E_{S\text{-}T}$ ($Au_{10}SG_{10}$) = 0.67 eV. For details on structures optimization see Computational Approach. Gold atoms in structures are labeled yellow. Ligands are detailed in windows of Fig. 2.

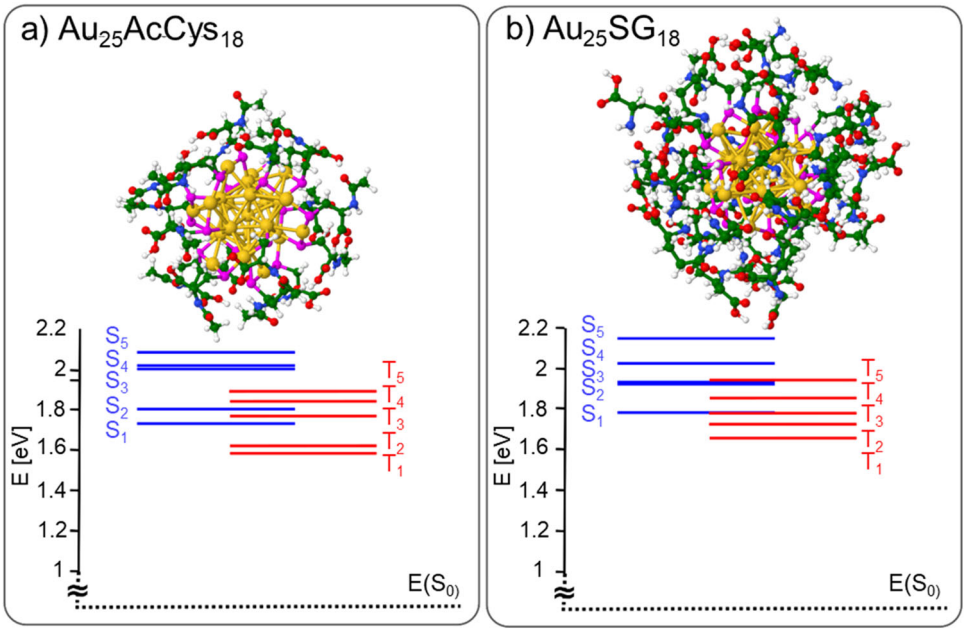

Fig. 5 Time-dependent density functional theory (TDDFT) energies for singlets (S_n, $n = 1$–5) and triplets (T_n, $n = 1$–5) states. TDDFT energies are shown for **a** $Au_{25}AcCys_{18}$ and **b** $Au_{25}SG_{18}$. Singlet-triplet (E_{S1}-E_{T1}) energy gaps are: $\Delta E_{S\text{-}T}$ ($Au_{25}AcCys_{18}$) = 0.15 eV and $\Delta E_{S\text{-}T}$ ($Au_{25}SG_{18}$) = 0.13 eV. For details on structures optimization see Computational Approach. Gold atoms in structures are labeled yellow. Ligands are detailed in windows of Fig. 3.

the gold core with delocalized electrons (Supplementary Fig. 5c, d). The influence of ligands on the relative energies of lowest singlet and triplet states is negligible since they do not participate in excitations. In contrast, size effect is pronounced due to the different structural properties.

The ability of Au_{10} and Au_{25} nanoclusters to generate reactive oxygen species in cells. Generation of reactive oxygen species (oxidants), including singlet oxygen, was determined in human microglia treated with the four ligated nanoclusters described above ($Au_{10}SG_{10}$, $Au_{10}AcCys_{10}$, $Au_{25}SG_{18}$, and $Au_{25}AcCys_{18}$). They did not significantly decrease cell viability after 24 h (Supplementary Fig. 6). Au_{10} generated small but detectable amounts of ROS without photoexcitation, whereas Au_{25} did not under similar conditions (Supplementary Fig. 7). In contrast, both one-photon (473 nm) and two-photon (720 nm) excitation of $Au_{25}AcCys_{18}$ causes an increase in ROS above endogenous levels.

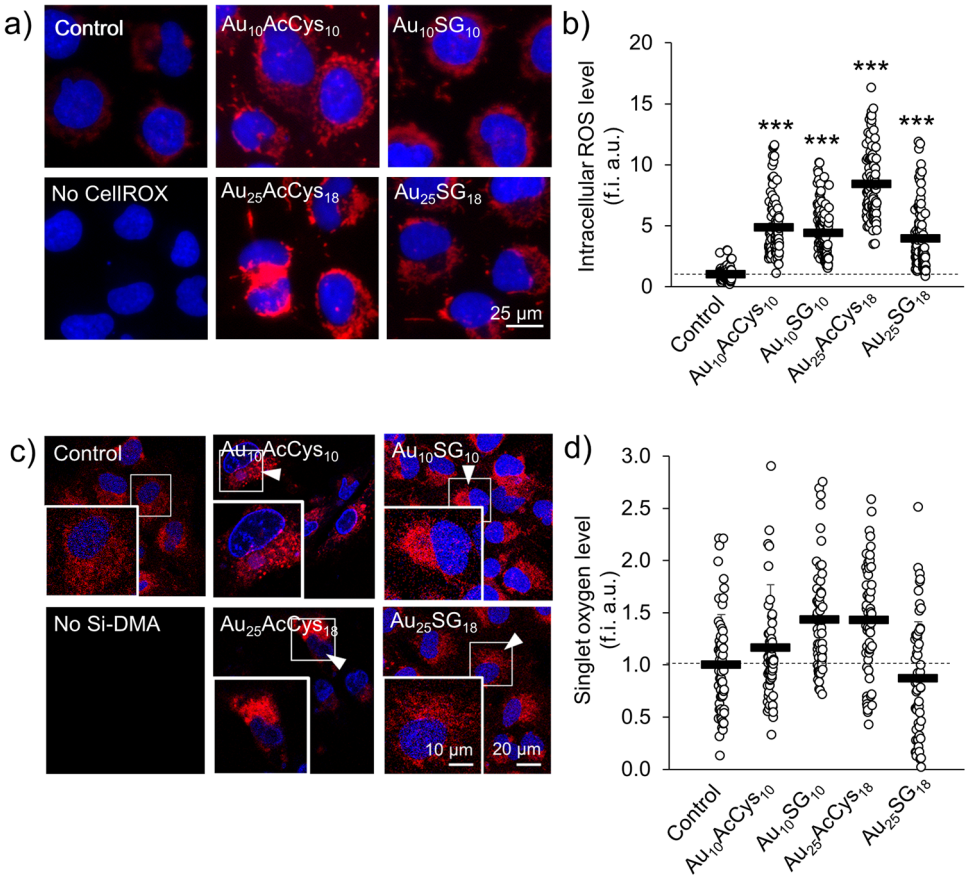

Fig. 6 Oxidative stress in human microglia in response to single- and two-photon-stimulated gold nanoclusters. a Representative fluorescence micrographs of ROS level in human microglia loaded with CellROX (red) and treated with $Au_{10}AcCys_{10}$, $Au_{10}SG_{10}$, $Au_{25}AcCys_{18}$ or $Au_{25}SG_{18}$ at 100 µM in serum-deprived conditions before stimulation with a one-photon laser (473 nm) for 3 min. Nuclei (blue) were labeled with Hoechst 33342. **b** Shown are the average level of ROS per individual cell (white dot) and the average ROS level per condition (black bar ±SD) in microglia treated as in a), normalized to the fluorescence intensity of the untreated control (set to 1). f.i. a.u. fluorescence intensity arbitrary units. At least 540 cells were analyzed from three independent experiments. **c** Representative fluorescence confocal micrographs of singlet oxygen levels (red, white arrows) in human microglia treated with gold nanoclusters $Au_{10}AcCys_{10}$, $Au_{10}SG_{10}$, $Au_{25}AcCys_{18}$, or $Au_{25}SG_{18}$ at 100 µM before exposure to two-photon laser (720 nm) for 3 min to induce singlet oxygen production. Singlet oxygen level was detected using the fluorescent probe Si-DMA. Nuclei (blue) are labeled with Hoechst 33342. **d** Shown are the average level of singlet oxygen in individual microglia cells (white dot) treated as in (**a**)), and the average level per condition (black bar), normalized to the fluorescence intensity prior to laser exposure (0 min, set to 1) from at least 60 cells per condition and at least two independent experiments. ***$p < 0.001$.

In particular, the abundance of singlet oxygen generated with two-photon excitation is markedly higher with $Au_{25}AcCys_{18}$ than with $Au_{25}SG_{18}$ (Fig. 6), complementing the theoretical part of this study.

Excessive ROS inadequately opposed by endogenous antioxidants results in oxidative stress. Several cellular mechanisms are activated in response to oxidative stress, including the master regulator of antioxidative response Nuclear factor-erythroid factor 2-related factor 2 (Nrf2). Nrf2 is a transcription factor retained in the cytosol by Kelch-like ECH-associated protein 1 (KEAP1) under basal conditions (Supplementary Fig. 8).

Oxidative stress causes Nrf2 to dissociate from KEAP1 and translocate to the nucleus to upregulate antioxidant proteins[31]. We examined the interaction of Nrf2 and KEAP1 in microglia exposed to the ligated gold nanoclusters using a proximity ligation assay, and found that $Au_{10}SG_{10}$ and $Au_{10}AcCys_{10}$, as well as $Au_{25}AcCys_{18}$, decreased the association of Nrf2 and KEAP1. The Supplementary Fig. 8b clearly shows the difference in ligand effect between SG and AcCys on Au_{25}, while such ligand effect is not observed for Au_{10}. SG does not contribute to the dissociation of the Nrf2-KEAP1 complex, whereas Au_{25} does. Untreated and acetyl-cysteine-treated cells served as controls. Acetyl-cysteine (100 µM or lower concentrations) did not have a significant effect on the complex dissociation (Supplementary Fig. 8b).

Discussion

In this study, we show that both the molecular-like properties of ultrasmall nanoclusters, as well as the nature of ligands affect the efficiency of gold clusters in solution to produce singlet oxygen upon excitation with visible light in a one-photon regime. Au_{25} nanoclusters with a gold core (and thus confined electrons) have a higher efficiency in generating $^1O_2$ than Au_{10} catenane structures with zero confined electrons. This behavior may be explained by (i) the excitation wavelength better matches the position of first singlet states in Au_{25} than in Au_{10}. In other words, the optical energy gap is inversely proportional to the number of confined electrons (the larger the number of confined electrons in the gold core, the smaller the optical gap)[32]. (ii) the S-T gap in Au_{25} is lower than in Au_{10}, making the intersystem crossing (ISC) process easier for Au_{25}. (iii) the energy gap (T_1-S_0) better matches the one of ligated Au_{25} than that of Au_{10} with the 0.98 eV energy required to generate $^1O_2$, thus facilitating the energy transfer process for Au_{25}.

The ligand nature also plays an important role in the capability to produce $^1O_2$ upon photoexcitation of nanoclusters. Acetyl-cysteine is more efficient than glutathione in attenuating $^1O_2$. This difference may be due to the structural motifs of surface ligands, in particular H-bond formation. Since glutathione is bulky and possesses both carboxylic groups and amine groups, a rich H-bond network formation is facilitated (Figs. 2 and 3), allowing better protection from solvent exposure[33]. The effect of a larger number of H-bonds is directly related to the flexibility of the ligated nanoclusters. Gold nanoclusters with acetyl-cysteine ligands are more flexible due to the smaller number of H-bonds, which enhances flexibility, thus increasing the probability of ISC between S and T states. This greater flexibility will induce a more efficient non-radiative relaxation and thus allowing for more efficient ISC between S and T states. Results from single-cell analyses upon treatment with the gold nanoclusters show that (1) Au_{10} is able to produce ROS with and without photoexcitation, but Au_{25} is able to produce ROS only with photoexcitation. (2) Formation of ROS leads to changes in the protein association between Nrf2 and KEAP1. Nrf2 is translocated to the nucleus when it dissociates from KEAP1[34,35]. This translocation turns on the activation of antioxidant genes as a protective mechanism against oxidative stress. We selected SG and acetyl-cysteine as ligands because these are endogenous compounds with established antioxidant effects[36,37]. These small compounds do not disturb cellular functions, as they are present endogenously in high concentrations. Interestingly, when attached to the gold nanoclusters, particularly Au_{25}, they show different effects. Possible interpretations for differences in biological effects in the production of ROS and Nrf2-KEAP1 response could be ascribed to the greater flexibility of $Au_{25}AcCys_{18}$ compared to $Au_{25}SG_{18}$. In line with the computational findings, surface ligands provide considerably greater amount of H-bonds in the case of $Au_{25}SG_{18}$ than with $Au_{25}AcCys_{18}$. This could result in the detachment of AcCys from the Au_{25} gold core more easily than for the surface ligand of $Au_{25}SG_{18}$. It is well documented that weakly attached ligands are replaced by intracellular SG, which is present in the 1–5 mM range.

We would like to point out here that experiments in solution and in cells were done with one- and two-photon excitation regimes, respectively. With two-photon excitation (at 720 nm, thus 1.72 eV), the terminal energy (e.g. 3.44 eV) would permit higher absorption for Au_{10} nanoclusters, thus opening more efficiently channels for de-excitation and the ISC process (compared to visible single-photon excitation). We cannot exclude that the relaxation pathways following one-photon excitation are different than that of two-photon excitation, as we demonstrated for the luminescence properties of Ag_{29} nanoclusters[38]. Such higher absorption and thus the opening of other channels for de-excitation and the ISC process might explain the singular behaviors observed in cells for Au_{10} nanoclusters— in particular $Au_{10}SG_{10}$. Clearly, a quantitative comparison of $^1O_2$ generation rate by Au_{10} and Au_{25} with two-photon excitation in solution would merit to be conducted. We managed to adapt the indirect method to measure ROS of nanoclusters in solution in the NLO regime. For this purpose, we verified the photostability of DPBF under high power femtosecond irradiation (see Supplementary Fig. 9). Then, we conducted ROS measurements in solution using the indirect method laser irradiation at 780 nm (for $Au_{25}SG_{18}$, $Au_{25}AcCys_{18}$ and $Au_{10}SG_{10}$) and at 720 nm (for $Au_{25}SG_{18}$, $Au_{25}AcCys_{18}$). To our knowledge, this is the first measurements of ROS efficiency in the NLO regime for nanoclusters. The $^1O_2$ generation rates of gold nanoclusters under a pulse laser irradiation at 780 nm and 720 nm are presented in Supplementary Table 2 (and Supplementary Fig. 10). Amazingly, both Au_{10} and Au_{25} NCs present efficient singlet oxygen generation rate under pulse 780 nm and 720 nm irradiation, and trends upon two-photon excitation (780 nm and 720) are similar to the one observed upon one-photon excitation (473 nm). In sum, our study presents an unprecedented, in-depth analysis of events taking place within gold nanoclusters when photoexcited from solution, to their possible biological consequences in living cells.

The principal aim of this study was to evaluate the possible ligand impact on ROS generation of photoexcited Au_{10} and Au_{25} nanoclusters. However, unopposed excess ROS leads to oxidative stress and deleterious effects in cells, which can be detected not only at/in the cell membranes, but also as diminished mitochondrial metabolic activity associated with morphological abnormalities, protein misfolding and aggregation, nuclear chromatin condensation, and shrinkage or disruption of the nuclear integrity. The choice of ligands (SG or AcCys) as protecting agents for gold clusters was mainly driven by their biocompatibility and their similarity from a biological point of view. In addition, our experimental-theoretical investigation has allowed to gain better insight into key factors (energetics of excited states (see Supplementary Table 3) and structural influence of surface ligands, in particular through hydrogen bonding networks) and their relative importance involved in singlet oxygen formation upon photoexcitation in the visible range. Altogether, this joint theoretical and experimental study allows to propose $Au_{25}AcCys_{18}$ ligated nanocluster as a good candidate for PDT. We also carried out live cell imaging to explore the ability of Au_{10} and Au_{25} nanoclusters to generate ROS in cells by one- and two-photon excitation. A deeper insight into the impact of nanoclusters on cell components (e.g. protein association between Nrf2 and KEAP1) was also reported.

A triangular strategy consisting of ligated photoexcited gold nanoclusters in solution and in living cells, combined with a theoretical approach for the structural and photophysical properties of nanoclusters with explicit ligands has been presented. This allowed for in-depth exploration of ROS generation by photoexcited nanoclusters at atomic precision, opening new routes for applications in PDT. Our studies focused on singlet oxygen species in living microglia cells, which surround the neurons and constitute a microenvironment of brain tumors. PDT employing Au_{25} nanoclusters would be of particular interest for brain tumor ablation without strongly disturbing the homeostasis of the microenvironment. To prove the usefulness of $Au_{25}AcCys_{18}$ for such a purpose, organoids with human cells would be an attractive biological model.

Methods

Au_{10} and Au_{25} cluster synthesis. All chemicals were commercially available and used without purification. $HAuCl_4{\cdot}3H_2O$, N-acetyl-L-cysteine (AcCys), and 1,3-diphenylisobenzofuran (DPBF) were purchased from Sigma-Aldrich. L-glutathione reduced, tributylamine, and triethylamine were procured from Carl Roth. Sodium borohydride was purchased from ACROS ORGANICS. Ammonia (NH_4OH), diethyl ether (Et_2O), and ethanol were purchased from VWR Chemicals. Methanol (MeOH) was purchased from Honeywell. New methylene blue (NMB) was purchased from TCI. Ultrapure Milli-Q water (resistivity 18.2 MΩ) was used for experimental purposes.

$Au_{10}SG_{10}$ and $Au_{25}SG_{18}$ nanoclusters were synthesized as reported by Bertorelle et al.[19] and by Ji et al.[39], respectively. $Au_{10}AcCys_{10}$ was synthesized as follow. 125 mg of L-Glutathione was dissolved in 35 mL of methanol and 2 mL of triethylamine. 100 mg of $HAuCl_4{\cdot}3H_2O$ in 15 mL of water was added and the solution was stirred overnight at ambient temperature. To complete precipitation, MeOH/Et_2O (volume rate 1:1) was added till precipitation. The dispersion was centrifuged. The powder was dissolved in a minimum of H_2O/NH_4OH solution and then precipitated with MeOH/Et_2O. The unwanted products were removed with cycles of dissolution/precipitation/centrifugation. After centrifugation, the powder was dissolved again in 10 mL of water. Then, 2 mL of glacial acetic acid was added and the solution was left undisturbed for 1 h. Pure $Au_{10}AcCys_{10}$ was precipitated and collected by centrifugation. A last cycle of dissolution/precipitation/centrifugation with H_2O/NH_4OH – MeOH/Et_2O was done before drying the powder.

For $Au_{25}AcCys_{18}$ synthesis,100 mg of gold salts ($HAuCl_4{\cdot}3H_2O$) was added to a solution of acetyl-cysteine (234 mg) dissolved in methanol (35 mL), followed by adding tributylamine (2 mL) and triethylamine (2 mL). After stirring for 5 min at room temperature, a first reducing agent was added (sodium borohydride, 3×25 mg spaced by 30 min). Then water (15 mL) and diethyl ether (15 mL) were added, followed by the addition of a second reducing agent (sodium borohydride, 4×50 mg spaced by 30 min). The solution was left undisturbed overnight before purification. Precipitation was induced by adding NH_4OH (1 mL, 10%), and the solution was centrifuged (9000 rpm). The unwanted products were removed with cycles of dissolution/precipitation/centrifugation. The powder was dissolved in a minimum of H_2O/NH_4OH, then precipitated with MeOH. After centrifugation, the powder was dissolved in water (10 mL), followed by adding glacial acetic acid (2 mL), then the solution was left undisturbed for 1 h before being centrifuged. The supernatant was collected and precipitated with MeOH. A last cycle of dissolution/precipitation with H_2O/NH_4OH and MeOH was done before drying the powder under vacuum.

Singlet oxygen generation and detection in solution. A 473 nm continuous wavelength laser (Changchun New Industries Optoelectronics Tech. Co., Ltd, China) with an output power of 250 mW and a beam diameter of 3 mm was used to photoexcite the nanoclusters in the linear optical regime. In the NLO regime, a Ti:Sapphire femtosecond laser (Coherent, Chameleon Ultra I) operating at 780 nm (720 nm) was used for two photon excitation with an irradiation power of 2.26 W (1.13 W) and a beam diameter of 1.2 mm. A typical solution used in the experiments contained nanoclusters and DPBF with a concentration of 1.37×10^{-6} M and 6.15×10^{-5} M, respectively. All solutions were prepared in ethanol. The samples were loaded in quartz cuvettes (1 cm light path length). Absorption spectra were recorded after photoexcitation of the nanoclusters with different times. The concentration of DPBF was calculated from the intensity of absorption peak at 412 nm according to the Beer–Lambert law. UV−vis absorption spectra were recorded on an Avantes AvaSpec-2048 spectrophotometer with an AvaLight DH-S deuterium lamp. Fluorescence emission spectra were recorded with a Horiba FluoroMax-4 spectrophotometer. Fluorescence lifetime was measured on a custom-built set-up[40]. The quantum yields of $Au_{10}AcCys_{10}$ and $Au_{25}AcCys_{18}$ were measured using $Au_{10}SG_{10}$ and $Au_{25}SG_{18}$ as references, respectively.

Cell culture. HMC3 human microglia were originally received from the American Type Culture Collection (ATCC). Unless otherwise indicated, cells were cultured in Dulbecco's Modified Eagle Medium (DMEM, Thermo Fisher Scientific) with 5% (v/v) fetal bovine serum (Wisent) and 1% (v/v) penicillin-streptomycin. Cells are kept at 37 °C with 5% CO_2 and 95% relative humidity. Cells tested negative for mycoplasma contamination.

Reactive oxygen species with one-photon stimulation. Reactive oxygen species in microglia stimulated with a one-photon laser was measured in cells seeded onto 12 mm glass coverslips (Assistant) at 7000 cells per coverslip, and cultured for 24 h. Cells were loaded with CellROX Deep Red (5 µM, Thermo Fisher Scientific) and Hoechst 33342 (10 µM, Millipore-Sigma) for 30 min at 37 °C, in phenol- and serum-free DMEM (Thermo Fisher Scientific). Cells were washed once in phenol- and serum-free DMEM before treatment with gold nanoclusters, and then exposure to a mercury laser (473 nm) for 3 min. Cells were imaged 5 min following laser exposure with a fluorescence microscope (Leica DMI4000 B). Fluorescence was analyzed in ImageJ (version 1.53t).

Singlet oxygen with two-photon stimulation. Microglia were seeded into 60 mm culture dishes (Fisher Scientific) at 20,000 cells per dish, and cultured for 24 h. Cells were washed twice with phosphate-buffered saline (PBS) before incubation with Si-DMA (50 nM, Thermo Fisher Scientific)[41,42] and Hoechst 33342 (10 µM) for 30 min at 37 °C in phenol-free Hank's Balanced Salt Solution (Thermo Fisher Scientific). Cells were washed once with Hank's Balanced Salt Solution, then treated with gold nanoclusters before stimulation with a Coherent Chameleon titanium-sapphire Multiphoton V2 laser IR two-photon laser (720 nm, 10% intensity, 80 MHz) for 3 min. Images were taken 5 min after laser exposure, with an argon 638 nm laser of a confocal microscope (Leica SP8). Fluorescence was analyzed in ImageJ.

Reactive oxygen species without photostimulation. Microglia were seeded onto 12 mm glass coverslips (Assistent) at 7000 cells per coverslip, and cultured for 24 h. Cells were washed twice with PBS before treatment with gold nanoclusters in serum-free DMEM. After treatment, cells were incubated with CellROX Deep Red (5 µM, Thermo Fisher Scientific) and Hoechst 33342 (10 µM, Millipore-Sigma) for 30 min at 37 °C, in phenol- and serum-free DMEM (Thermo Fisher Scientific). Cells were washed once in phenol- and serum-free DMEM before imaging with a fluorescence microscope (Leica DMI4000 B). Fluorescence was analyzed in ImageJ (version 1.53t).

Proximity ligation assay. Microglia were seeded and treated as for the detection of reactive oxygen species. After treatment, cells were washed twice with PBS and fixed with 4% (w/v) paraformaldehyde (BDH) for 10 min. Cells were permeabilized with 0.1% (v/v) Triton X-100 (Millipore-Sigma) in PBS for 10 min. The proximity ligation assay was performed following the manufacturer's protocol for Duolink (Millipore-Sigma) and using primary antibodies against Nrf2 (rabbit, 1/500, ab31163, Abcam) and KEAP1 (mouse, 1/500, 4G10H9, Proteintech) for 24 h at 4 °C. Cells were then incubated with Phalloidin Alexa Fluor 488 (1X, Thermo Fisher Scientific) and Hoechst 33342 (10 µM) for 20 min in PBS, washed twice with PBS, and mounted onto microscope slides (Fisher Scientific) using Aqua-Poly/Mount (Polysciences). Cells were imaged using a fluorescence microscope (Leica DMI4000 B).

Cell viability. Cells were seeded onto glass coverslips at 10,000 cells per coverslip and incubated for 24 h before treatment. Cells were treated with gold nanoclusters as for the measurement of reactive oxygen species. After treatment, cells were fixed with 4% paraformaldehyde (10 min), permeabilized with 0.1% Triton X-100 (10 min), and nuclei were labeled with Hoechst 33342 (10 µM, 10 min). Cells were washed twice with PBS, then mounted onto microscope slides using Aqua-Poly/Mount. Cells were imaged using a fluorescence microscope (Leica DMI4000 B).

Statistics. One-way ANOVA with Tukey-Kramer's post-hoc test was performed. In accordance to the Central Limit Theorem, sample sizes larger than 30 were assumed to have a normal distribution. Equality of variance was verified by Levene's test. A p-value lower than 0.05 indicated statistical significance.

Computational approach. Density functional theory (DFT) has been used to determine the structural properties of liganded AuNCs: $Au_{25}(SCH3)_{18}$ and $Au_{10}(SCH_3)_{10}$. The optimization of structures was performed with PBE functional[43,44] implemented in Gaussian computational chemistry software. Coordinates for the starting structure of $Au_{25}(SCH3)_{18}$ were taken from crystal structure of $Au_{25}(SCH2CH2Ph)_{18}$[45] as well as from previously optimized DFT structure[46], and the coordinates for the starting structure of $Au_{10}(SCH_3)_{10}$ were taken from previously optimized DFT structure[19,47]. Semiempirical method PM7[48] has been used to optimize the AuNCs structures with full ligands, by freezing the coordinates of gold and sulfur atoms to ensure that Au-Au and Au-S bond distances remain unchanged with respect to previously obtained bond distances from DFT structures of $Au_{10}(SCH_3)_{10}$ and $Au_{25}(SCH3)18$. Structures with full ligands were used in calculations of excited state properties within time-dependent density functional (TDDFT) method. Relativistic effective core potential[46] of the Stuttgart group was employed for gold atoms. For gold and sulfur atoms SVP AO basis set[49], and for other atoms of ligands 3-21 G AO's basis set was used[50,51]. Singlet and triplet states were obtained using the TDDFT and Coulomb-attenuated version of Becke's three-parameter non-local exchange functional together with the Lee–Yang–Parr gradient-corrected correlation functional[52] implemented in Gaussian[53]. Restricted TDDFT approach has also been employed for calculation of triplet states. The $\Delta E_{S\text{-}T}$ obtained from unrestricted TDDFT show the same trend: $\Delta E_{S\text{-}T}$ is larger for $Au_{10}SG_{10}$, $Au_{10}AcCys_{10}$, then for $Au_{25}SG_{18}$, $Au_{25}AcCys_{18}$. Size effect due to structural difference is dominant. Effect of different ligands on the given cluster size is negligible for linear optical properties because ligands do not participate in excitations. Consideration of organization of ligands using molecular dynamic simulations is relevant in the context of aggregation and fibrillation[54,55]. Inclusion of solvent doesn't have major impact on geometries since the changes in average distance are not larger than 0.010 Å.

Data availability

The data supporting the findings of this study are available upon reasonable request from the corresponding authors.

Received: 21 December 2022; Accepted: 4 May 2023;
Published online: 22 May 2023

References

1. Sies, H. et al. Defining roles of specific reactive oxygen species (ROS) in cell biology and physiology. *Nat. Rev. Mol. Cell Biol.* **23**, 499–515 (2022).
2. Escudero, A. et al. Photodynamic therapy: photosensitizers and nanostructures. *Mater. Chem. Front.* **5**, 3788–3812 (2021).
3. Monsour, C. G., Decosto, C. M., Tafolla-Aguirre, B. J., Morales, L. A. & Selke, M. Singlet oxygen generation, quenching and reactivity with metal thiolates. *Photochem. Photobiol.* **97**, 1219–1240 (2021).
4. Lan, M. et al. Photosensitizers for Photodynamic Therapy. *Adv. Healthc. Mater.* **8**, 1900132 (2019).
5. Qian, H., Zhu, M., Wu, Z. & Jin, R. Quantum sized gold nanoclusters with atomic precision. *Acc. Chem. Res.* **45**, 1470–1479 (2012).
6. Bonačić-Koutecký, V. & Antoine, R. Enhanced two-photon absorption of ligated silver and gold nanoclusters: theoretical and experimental assessments. *Nanoscale* **11**, 12436–12448 (2019).

7. Kawasaki, H. et al. Generation of singlet oxygen by photoexcited Au25(SR)18 clusters. *Chem. Mater.* **26**, 2777–2788 (2014).
8. Ho-Wu, R., Yau, S. H. & Goodson, T. III Efficient singlet oxygen generation in metal nanoclusters for two-photon photodynamic therapy applications. *J. Phys. Chem. B* **121**, 10073–10080 (2017).
9. Kawamura, K. et al. Ultrasonic activation of water-soluble au25(sr)18 nanoclusters for singlet oxygen production. *J. Phys. Chem. C* **123**, 26644–26652 (2019).
10. Poderys, V., Jarockyte, G., Bagdonas, S., Karabanovas, V. & Rotomskis, R. Protein-stabilized gold nanoclusters for PDT: ROS and singlet oxygen generation. *J. Photochem. Photobiol. B: Biol.* **204**, 111802 (2020).
11. Dan, Q. et al. Gold nanoclusters-based NIR-II photosensitizers with catalase-like activity for boosted photodynamic therapy. *Pharmaceutics* **14**, 1645 (2022).
12. Lillo, C. R. et al. BSA-capped gold nanoclusters as potential theragnostic for skin diseases: photoactivation, skin penetration, in vitro, and in vivo toxicity. *Mater. Sci. Eng.: C* **112**, 110891 (2020).
13. Dan, Q. et al. Ultrasmall theranostic nanozymes to modulate tumor hypoxia for augmenting photodynamic therapy and radiotherapy. *Biomater. Sci.* **8**, 973–987 (2020).
14. Geng, T. et al. Bovine serum albumin-encapsulated ultrasmall gold nanoclusters for photodynamic therapy of tumors. *ACS Appl. Nano Mater.* **4**, 13818–13825 (2021).
15. Han, R. et al. Super-efficient in vivo two-photon photodynamic therapy with a gold nanocluster as a type I photosensitizer. *ACS Nano* **14**, 9532–9544 (2020).
16. Yagi, J., Ikeda, A., Wang, L.-C., Yeh, C.-S. & Kawasaki, H. Singlet oxygen generation using thiolated gold nanoclusters under photo- and ultrasonic excitation: size and ligand effect. *J. Phys. Chem. C* **126**, 19693–19704 (2022).
17. Negishi, Y., Nobusada, K. & Tsukuda, T. Glutathione-protected gold clusters revisited: bridging the gap between gold(i)−thiolate complexes and thiolate-protected gold nanocrystals. *J. Am. Chem. Soc.* **127**, 5261–5270 (2005).
18. Kang, X., Chong, H. & Zhu, M. Au25(SR)18: the captain of the great nanocluster ship. *Nanoscale* **10**, 10758–10834 (2018).
19. Bertorelle, F. et al. Au10(SG)10: a chiral gold catenane nanocluster with zero confined electrons. optical properties and first-principles theoretical analysis. *J. Phys. Chem. Lett.* **8**, 1979–1985 (2017).
20. Comby-Zerbino, C. et al. Catenane structures of homoleptic thioglycolic acid-protected gold nanoclusters evidenced by ion mobility-mass spectrometry and DFT calculations. *Nanomaterials* **9**, 457 (2019).
21. Comby-Zerbino, C., Bertorelle, F., Chirot, F., Dugourd, P. & Antoine, R. Structural insights into glutathione-protected gold Au10−12(SG)10−12 nanoclusters revealed by ion mobility mass spectrometry. *Eur. Phys. J. D.* **72**, 144 (2018).
22. Basu, S. et al. Rationale strategy to tune the optical properties of gold catenane nanoclusters by doping with silver atoms. *J. Phys. Chem. C* **124**, 19368–19374 (2020).
23. Wu, Z. & Jin, R. On the ligand's role in the fluorescence of gold nanoclusters. *Nano Lett.* **10**, 2568–2573 (2010).
24. Yamamoto, M. et al. Effects of ligand species and cluster size of biomolecule-protected Au nanoclusters on efficiency of singlet-oxygen generation. *J. Lumin.* **180**, 315–320 (2016).
25. Comby-Zerbino, C., Dagany, X., Chirot, F., Dugourd, P. & Antoine, R. The emergence of mass spectrometry for characterizing nanomaterials. Atomically precise nanoclusters and beyond. *Mater. Adv.* **2**, 4896–4913 (2021).
26. Mlejnek, P. Direct interaction between N-acetylcysteine and cytotoxic electrophile—an overlooked in vitro mechanism of protection. *Antioxidants* **11**, 1485 (2022).
27. Maysinger, D. et al. Insights into the impact of gold nanoclusters Au10SG10 on human microglia. *ACS Chem. Neurosci.* **13**, 464–476 (2022).
28. Entradas, T., Waldron, S. & Volk, M. The detection sensitivity of commonly used singlet oxygen probes in aqueous environments. *J. Photochem. Photobiol. B: Biol.* **204**, 111787 (2020).
29. Polavarapu, L., Manna, M. & Xu, Q.-H. Biocompatible glutathione capped gold clusters as one- and two-photon excitation fluorescence contrast agents for live cells imaging. *Nanoscale* **3**, 429–434 (2011).
30. Ramakrishna, G., Varnavski, O., Kim, J., Lee, D. & Goodson, T. Quantum-sized gold clusters as efficient two-photon absorbers. *J. Am. Chem. Soc.* **130**, 5032–5033 (2008).
31. Bellezza, I., Giambanco, I., Minelli, A. & Donato, R. Nrf2-Keap1 signaling in oxidative and reductive stress. *Biochim. Biophys. Acta Mol. Cell Res.* **1865**, 721–733 (2018).
32. Jin, R. Atomically precise metal nanoclusters: stable sizes and optical properties. *Nanoscale* **7**, 1549–1565 (2015).
33. Perić, M. et al. Ligand shell size effects on one- and two-photon excitation fluorescence of zwitterion functionalized gold nanoclusters. *Phys. Chem. Chem. Phys.* **21**, 23916–23921 (2019).
34. Baird, L. & Yamamoto, M. The molecular mechanisms regulating the KEAP1-NRF2 pathway. *Mol. Cell. Biol.* **40**, e00099–00020 (2020).
35. Suzuki, T. et al. Molecular mechanism of cellular oxidative stress sensing by Keap1. *Cell Rep.* **28**, 746–758.e744 (2019).
36. Gaucher, C. et al. Glutathione: antioxidant properties dedicated to nanotechnologies. *Antioxidants* **7**, 62 (2018).
37. Pedre, B., Barayeu, U., Ezeriņa, D. & Dick, T. P. The mechanism of action of N-acetylcysteine (NAC): the emerging role of H2S and sulfane sulfur species. *Pharmacol. Ther.* **228**, 107916 (2021).
38. Russier-Antoine, I. et al. Tuning Ag29 nanocluster light emission from red to blue with one and two-photon excitation. *Nanoscale* **8**, 2892–2898 (2016).
39. Ji, J. et al. Organotypic and primary neural cultures as models to assess effects of different gold nanostructures on glia and neurons. *Nanotoxicology* **13**, 285–304 (2019).
40. Soleilhac, A., Dagany, X., Dugourd, P., Girod, M. & Antoine, R. Correlating droplet size with temperature changes in electrospray source by optical methods. *Anal. Chem.* **87**, 8210–8217 (2015).
41. Murotomi, K., Umeno, A., Sugino, S. & Yoshida, Y. Quantitative kinetics of intracellular singlet oxygen generation using a fluorescence probe. *Sci. Rep.* **10**, 10616 (2020).
42. Liu, H.-W. et al. An efficient two-photon fluorescent probe for monitoring mitochondrial singlet oxygen in tissues during photodynamic therapy. *Chem. Commun.* **52**, 12330–12333 (2016).
43. Perdew, J. P., Ernzerhof, M. & Burke, K. Rationale for mixing exact exchange with density functional approximations. *J. Chem. Phys.* **105**, 9982–9985 (1996).
44. Perdew, J. P. et al. Atoms, molecules, solids, and surfaces: applications of the generalized gradient approximation for exchange and correlation. *Phys. Rev. B* **46**, 6671–6687 (1992).
45. Zhu, M., Aikens, C. M., Hollander, F. J., Schatz, G. C. & Jin, R. Correlating the crystal structure of A thiol-protected Au25 cluster and optical properties. *J. Am. Chem. Soc.* **130**, 5883–5885 (2008).
46. Dolg, M., Stoll, H. & Preuss, H. Energy-adjusted ab initio pseudopotentials for the rare earth elements. *J. Chem. Phys.* **90**, 1730–1734 (1989).
47. Liu, Y., Tian, Z. & Cheng, L. Size evolution and ligand effects on the structures and stability of (AuL)n (L = Cl, SH, SCH3, PH2, P(CH3)2, n = 1–13) clusters. *RSC Adv.* **6**, 4705–4712 (2016).
48. Stewart, J. J. P. Optimization of parameters for semiempirical methods VI: more modifications to the NDDO approximations and re-optimization of parameters. *J. Mol. Modeling* **19**, 1–32 (2013).
49. Weigend, F. & Ahlrichs, R. Balanced basis sets of split valence, triple zeta valence and quadruple zeta valence quality for H to Rn: design and assessment of accuracy. *Phys. Chem. Chem. Phys.* **7**, 3297–3305 (2005).
50. Binkley, J. S., Pople, J. A. & Hehre, W. J. Self-consistent molecular orbital methods. 21. Small split-valence basis sets for first-row elements. *J. Am. Chem. Soc.* **102**, 939–947 (1980).
51. Dobbs, K. D. & Hehre, W. J. Molecular orbital theory of the properties of inorganic and organometallic compounds. 6. Extended basis sets for second-row transition metals. *J. Comput. Chem.* **8**, 880–893 (1987).
52. Yanai, T., Tew, D. P. & Handy, N. C. A new hybrid exchange–correlation functional using the Coulomb-attenuating method (CAM-B3LYP). *Chem. Phys. Lett.* **393**, 51–57 (2004).
53. Frisch, M. J. et al. Gaussian 16 Rev. C.01.) (2016).
54. Brancolini, G., Toroz, D. & Corni, S. Can small hydrophobic gold nanoparticles inhibit β2-microglobulin fibrillation? *Nanoscale* **6**, 7903–7911 (2014).
55. Vanzan, M., Rosa, M. & Corni, S. Atomistic insight into the aggregation of [Au25(SR)18]q nanoclusters. *Nanoscale Adv.* **2**, 2842–2852 (2020).
56. Ronzani, F. et al. Comparison of the photophysical properties of three phenothiazine derivatives: transient detection and singlet oxygen production. *Photochem. Photobiol. Sci.* **12**, 2160–2169 (2013).

Acknowledgements

This research was supported by the project STIM-REI, Contract Number: KK.01.1.1.01.0003, funded by the European Union through the European Regional Development Fund–the Operational Programme Competitiveness and Cohesion 2014–2020 (KK.01.1.1.01). V.B.K., M.P.B., Z.S.M., and H.F. acknowledge computational facilities of the HPC computer within the STIM-REI project, Doctoral study of Biophysics at the University of Split as well as Prof. Miroslav Radman at MedILS and Split-Dalmatia County for support. H.Y. is grateful for PhD fellowships donated by the China Scholarship Council (CSC). D.B. is grateful for post-doc fellowship donated by Agence Nationale de la Recherche (project MANBAMM, ANR-21-CE29-0020). R.A. and H.Y. acknowledge Shanghai Science and Technology Innovation Program (22520712500) for support. We gratefully acknowledge Marion Girod (Institut des Sciences Analytiques, Villerbanne, France) for lending us the continuous wave 473 nm laser. D.M. acknowledges funding from NSERC (RGPIN 2020-07011).

Author contributions

R.A., V.B.K., and D.M. conceived the initial idea and coordinated the work. H.F. synthesized and prepared the nanoclusters, assisted with H.Y. and D.B. H.F. recorded and analyzed mass spectra. H.Y. conducted ROS experiments with nanoclusters in solution upon one-photon

excitation, supervised by H.F. and R.A. H.Y. and D.B. conducted ROS experiments with nanoclusters in solution upon two-photon excitation, supervised by F.R. and P.F.B. I.Z. conducted ROS experiments with nanoclusters in cells, supervised by D.M. M.P.B., Z.S.M., and V.B.K. performed and analyzed the theoretical results. R.A., V.B.K., and D.M. supervised and financed the project. R.A., V.B.K., and D.M. wrote the paper. All authors provided critical feedback and helped to shape the final manuscript.

Competing interests

R.A. is a Guest Editor for Communications Chemistry's Atomically precise nanochemistry Collection, but was not involved in the editorial review of, or the decision to publish this article. All other authors declare no competing interests.

Additional information

Supplementary information The online version contains supplementary material available at https://doi.org/10.1038/s42004-023-00895-5.

Correspondence and requests for materials should be addressed to Rodolphe Antoine, Vlasta Bonačić-Koutecký or Dusica Maysinger.

Peer review information *Communications Chemistry* thanks Hideya Kawasaki and the other, anonymous, reviewers for their contribution to the peer review of this work.

Reprints and permission information is available at http://www.nature.com/reprints

Publisher's note Springer Nature remains neutral with regard to jurisdictional claims in published maps and institutional affiliations.